ADVANCED FUNCTIONAL MATERIALS

www.afm-journal.de

Ultrasound-Induced Wireless Energy Harvesting for Potential Retinal Electrical Stimulation Application

Laiming Jiang, Yang Yang, Ruimin Chen, Gengxi Lu, Runze Li, Jie Xing, K. Kirk Shung, Mark S. Humayun, Jianguo Zhu,* Yong Chen,* and Qifa Zhou**

Retinal electrical stimulation for people with neurodegenerative diseases has shown to be feasible for direct excitation of neurons as a means of restoring vision. In this work, a new electrical stimulation strategy is proposed using ultrasound-driven wireless energy harvesting technology to convert acoustic energy to electricity through the piezoelectric effect. The design, fabrication, and performance of a millimeter-scale flexible ultrasound patch that utilizes an environment-friendly lead-free piezocomposite are described. A modified dice-and-fill technique is used to manufacture the microstructure of the piezocomposite and to generate improved electrical and acoustic properties. The as-developed device can be attached on a complex surface and be driven by ultrasound to produce adjustable electrical outputs, reaching a maximum output power of 45 mW cm^{-2}. Potential applications for charging energy storage devices and powering commercial electronics using the device are demonstrated. The considerable current signals (e.g., current >72 µA and current density >9.2 nA µm^{-2}) that are higher than the average thresholds of retinal stimulation are also obtained in the ex vivo experiment of an implanted environment, showing great potential to be integrated on implanted biomedical devices for electrical stimulation application.

1. Introduction

Visual prostheses to produce a sense of image by electrically exciting neurons in the visual system have shown incredible promise, enabling those blind to perceive visual signals from the devastating outer retinal diseases,[1–3] such as retinitis pigmentosa where the photoreceptors are damaged but the remaining inner retinal circuitry remains mostly intact.[4] A visual prosthesis system comprises an external or implantable imaging system that acquires and processes the image. Power and data are transferred to the implant by an external unit. The implant receives power and delivers the data to the nerve through the microelectrodes.[5,6] Thus, a power transfer system that is capable of providing sufficient energy for neural stimulation within security limits is needed that also ensure the device's portability, biocompatibility, and longevity. Wireless power technology is therefore of great interest as it plays a vital role in eliminating the invasiveness and discomfort caused by batteries or wires in most implantable medical devices.[7,8] Recently, wireless devices capable of achieving untethered transfer, as well as mm-scale integrated circuits for neuro-stimulation have been developed.[9] Nevertheless, most wireless power systems employ electromagnetic energy coupling, which turns out to be extremely inefficient in mm (or micro)-scale systems due to the mismatch between the radio wavelength (≈cm) and aperture of mm-scale receivers.[10,11] New approaches are required for the further miniaturization of wireless electronic platforms that are capable of effectively interfacing with small nerve bundles.

Here we propose a new electrical stimulation strategy of using the ultrasound-induced energy for wirelessly powering mm-scale implants. Our strategy begins by designing a delicate architecture assembled from an ultrasound transmitter and an

---

L. Jiang, R. Li, Prof. M. S. Humayun, Prof. Q. Zhou
Roski Eye Institute
Keck School of Medicine
University of Southern California
Los Angeles, CA 90033, USA
E-mail: qifazhou@usc.edu

L. Jiang, Dr. J. Xing, Prof. J. Zhu
College of Materials Science and Engineering
Sichuan University
Chengdu 610064, China
E-mail: nic0400@scu.edu.cn

Dr. Y. Yang, Prof. Y. Chen
Epstein Department of Industrial and Systems Engineering
Department of Aerospace and Mechanical Engineering
Viterbi School of Engineering
University of Southern California
Los Angeles, CA 90089, USA
E-mail: yang610@usc.edu; yongchen@usc.edu

Dr. Y. Yang
Department of Mechanical Engineering
San Diego State University
5500 Campanile Drive, San Diego, CA 92182, USA

Dr. R. Chen, G. Lu, R. Li, Prof. K. K. Shung, Prof. Q. Zhou
Department of Biomedical Engineering
Viterbi School of Engineering
University of Southern California
Los Angeles, CA 90089, USA

The ORCID identification number(s) for the author(s) of this article can be found under https://doi.org/10.1002/adfm.201902522.

DOI: 10.1002/adfm.201902522

ultrasound receiver, which allows us to manipulate the conversion of electroacoustics by the piezoelectric effect,[12] thereby achieving the control of the electrical stimulation energy. In contrast to electromagnetic coupling, ultrasound for power transfer possesses several major advantages. First, the acoustic velocity (c) is five orders of magnitude lower than that of radio in tissue, resulting in much smaller wavelengths ($c = \lambda f$) at similar frequencies (f). The velocity difference allows the energy to be focused to a millimeter spot size, yielding an excellent spatial resolution.[13,14] Second, the attenuation of acoustic energy in tissue is much less than that of electromagnetic radiation.[11,15] This not only results in a higher traveling depth for a given power but also significantly reduces unnecessary power losses due to scattering or absorption of tissue. Third, ultrasound is safer in most cases.[16] Ultrasound technology has long been applied for medical diagnosis and therapeutics.[17–19] According to the Food and Drug Administration (FDA), a limited ultrasound intensity of 720 $\text{mW} \cdot \text{cm}^{-2}$ is permissible into the human body for diagnostic applications,[20] which is two orders of magnitude higher than the safety threshold (1–10 $\text{mW} \cdot \text{cm}^{-2}$) of radio waves.[21] Therefore, the wireless energy transfer technology that is ultrasonically driven is a promising strategy. For example, Seo and Johnson et al. have reported an ultrasonic neural dust system for peripheral nerve stimulation and recording, which performs downlink communication and readout through ultrasonic power and control.[11,22] However, their design presents a rigid structure that employs toxic lead-based piezoelectric materials as a core element. These drawbacks represent a common obstacle for the development of advanced bio-implants that can combine excellent soft mechanical performance with environmental friendliness to ensure the harmlessness to the human body in long-term implantation.

In this work, we prepare an anisotropic 1-3 type lead-free piezocomposite that is integrated into an mm-scale flexible format with a flexible electrode for external contact and a silicone elastomer for encapsulation.[23] The as-developed lead-free piezoelectric ultrasonic energy harvester (LF-PUEH) is capable of being implanted into eyeballs to sense the transmitted ultrasonic signals from a few centimeters away and to convert them into usable electrical signals. Achieving improved acoustic and electrical properties and similar mechanical properties to the tissue, the flexible ultrasound patch not only achieves a high piezoelectric potential under ultrasonic drive but also simultaneously possess environmental friendliness and high flexibility to ensure a safe and intimate contact with the time-varying tissue surface. Systematic studies including frequency characteristics, input conditions, load optimization, and implant mimic are implemented to evaluate its output characteristics and to demonstrate its use in potential applications. The study paves the way for a future generation of an eco-friendly implantable electric stimulation device, thus moving the ultrasound-driven energy transfer technology towards real-world applications.[24,25]

2. Results and Discussion

The as-developed LF-PUEH device hybridizes high-performance microscale piezocomposite with flexible structural components. The schematic of the device is presented in **Figure 1**a. As the core component of an ultrasonic energy harvester (UEH) device, the anisotropic 1-3 piezocomposite that combines the desirable performance of two different phases possesses better electromechanical coupling than the isotropic piezoelectric materials in ultrasonic energy transfer applications.[12,26] The idea has proven to be effective in developing 1-3 type piezocomposite composed of piezoelectric array and piezoelectric inactive polymer.[27,28] Currently, lead-based piezoelectric materials represented by lead zirconate titanate ceramics and the related lead-based perovskites are dominant in the piezoceramic market because of their good piezoelectric properties. Nevertheless, due to the biohazard regarding the current lead-based piezoelectric materials and express provisions of Restriction of Hazardous Substances,[29] the attention has been shifted to lead-free alternatives, especially on potassium-sodium niobate-based piezoelectrics.[30–33] In this work, a new 1-3 piezocomposite comprising a system of high piezoelectricity lead-free ceramic [$(K_{0.48}Na_{0.52})(Nb_{0.95}Sb_{0.05})O_3$-$(Bi_{0.4}La_{0.1})(Na_{0.4}Li_{0.1})ZrO_3$, abbreviated as KNNS] pillar array with parallelepipeds shape and the insulating polymer filler (EPO-TEK 301) was designed and fabricated using a modified dice-and-fill technique (**Figure 2**a).[34] As displayed in the scanning electron microscopy (SEM) micrograph (Figure 2b) and X-ray diffraction (XRD) pattern (Figure 2f), the prepared KNNS sample exhibits a dense ceramic body and a typical perovskite structure with a multiphase coexisting state, ensuring excellent properties of the material. According to the parallel and series model proposed by Chan et al.,[28] the acoustic and electrical properties of the composite can be predicted theoretically (Figure S1, Supporting Information). The electromechanical coupling coefficient k_{33}, voltage coefficient g_{33}, piezoelectric coefficient d_{33}, permittivity ε_{33}^{T}, and acoustic impedance Z_a are determined as a function of KNNS volume fraction (ν) by the following equations:

$$k_{33} = \sqrt{1 - C_{33}^{E}/C_{33}^{D}} \tag{1}$$

$$g_{33} = d_{33}/\varepsilon_{33}^{T} \tag{2}$$

$$d_{33} = \nu s_{11,\text{epoxy}}^{P} d_{33,\text{KNNS}}/S(\nu) \tag{3}$$

$$\varepsilon_{33}^{T} = \nu \varepsilon_{33,\text{KNNS}}^{T} - \nu(1-\nu)\left(d_{33,\text{KNNS}}\right)^{2}/S(\nu) + (1-\nu)\varepsilon_{11,\text{epoxy}}^{P} \tag{4}$$

$$Z_{\text{a}} = \sqrt{\rho \times C_{33}^{D}} \tag{5}$$

wherein $S(\nu) = \nu s_{11,\text{epoxy}}^{P} + (1-\nu) s_{33,\text{KNNS}}^{E}$, ρ is the density, s is the elastic compliance, and C is the elastic stiffness. In addition, several guidelines are followed to improve the harvester performance when designing the spatial dimensions of the 1-3 piezoelectric composite. First, a width-to-thickness aspect ratio of less than 0.5 is required for the KNNS pillar because the half-wave lateral mode of the piezoelectric pillars should be well above the fundamental thickness vibration so that their harmonics do not couple to the thickness mode.[35] Second, the stopband edge resonant frequency should be higher than twice

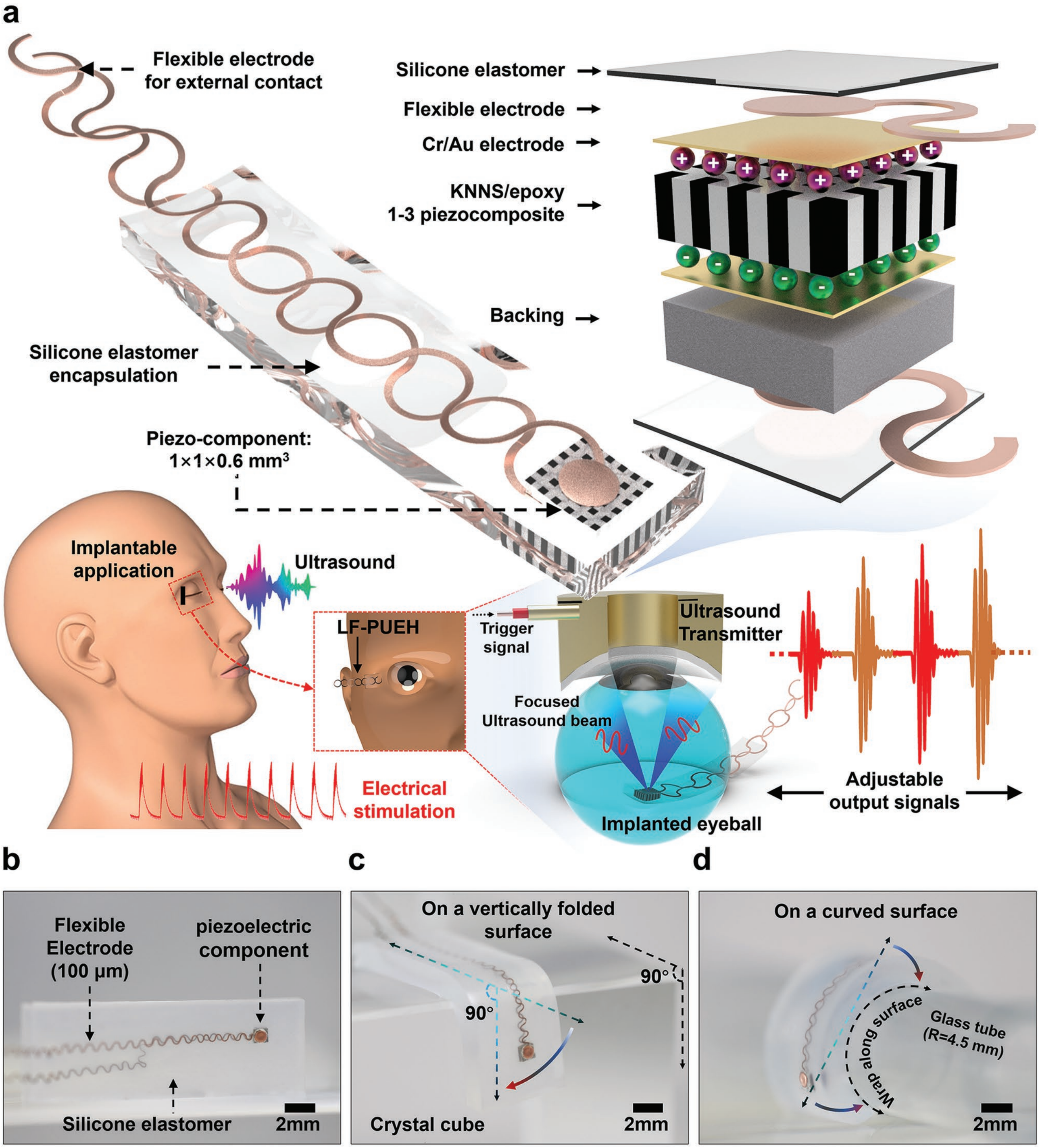

Figure 1. Schematic and design of the mm-scale flexible LF-PUEH device. a) Schematics of the device, with key components labeled. The device employs an environmentally friendly lead-free piezocomposite as the core component, wavy-structure-based flexible electrodes for external contact, and a silicone elastomer for encapsulation. The device can be driven by the ultrasound to produce adjustable electrical outputs for electrical stimulation applications. b–d) Optical images of the device when it stands freely, wraps over a vertically folded surface, and a curved surface, demonstrating the mechanical compliance of the device.

the fundamental thickness resonant frequency.[36] Thus, the spacing between KNNS pillars should be less than $c_s/2f$, where c_s and f are the shear wave velocity of the polymer fillers and the thickness resonant frequency of the pillars, respectively. Based on the above theoretical analysis, a ceramic/polymer piezocomposite with the miniaturized piezoelectric pillars (85 µm × 85 µm × 300 µm) and kerfs (25 µm) was designed and fabricated (Figure 2b–e; Figure S2, Supporting Information),

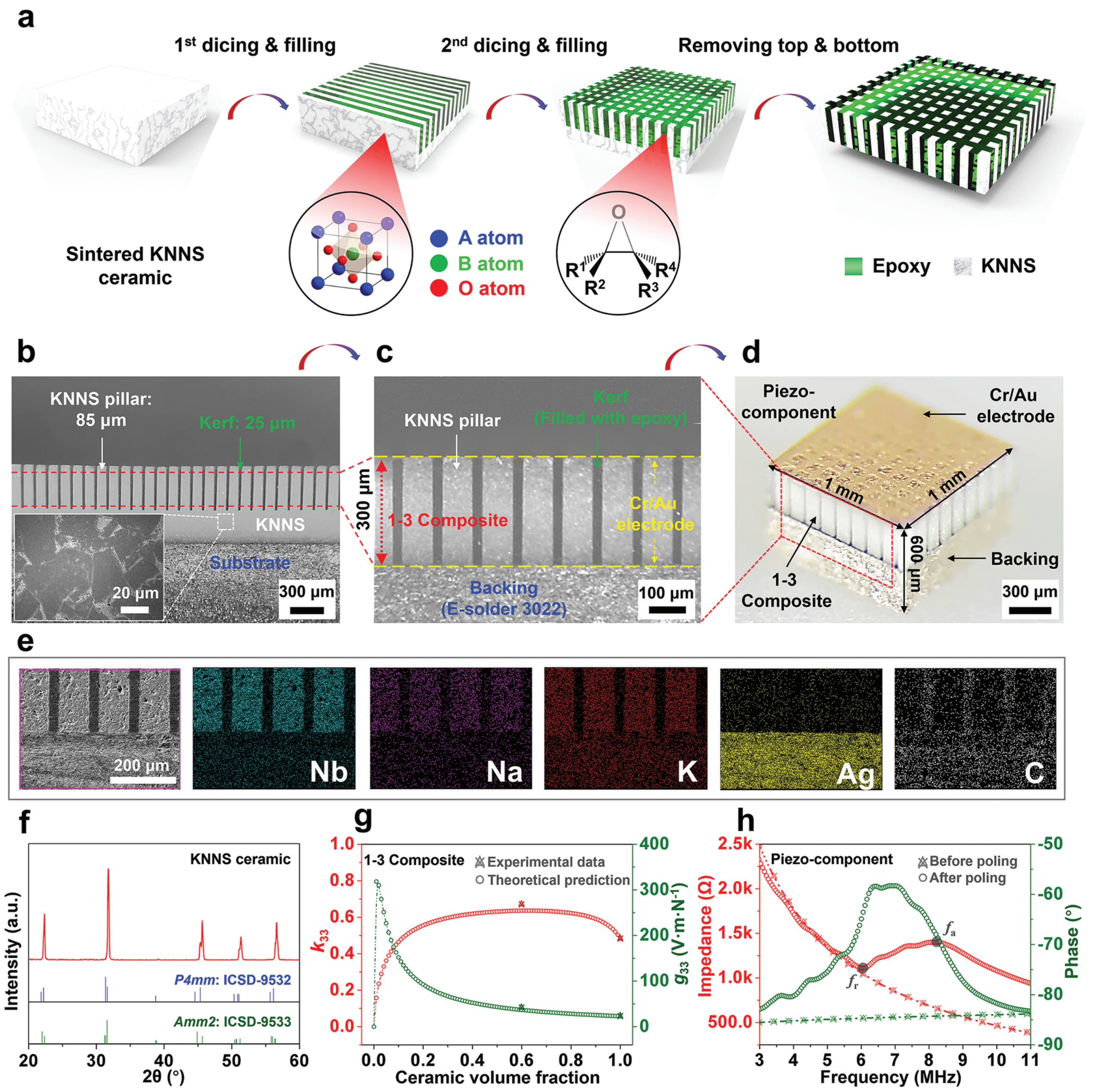

Figure 2. Fabrication and characterization of the 1-3 piezocomposite component. a) Schematic illustration of the process of preparing the 1-3 ceramic/polymer piezocomposite using a modified dice-and-fill technique. b) Optical image of the KNNS ceramic pillars array after dicing. The inset shows the SEM micrograph of KNNS ceramic. c,d) Optical images of the prepared piezo-component with a backing layer after lapping to the required thickness. e) Energy dispersive spectroscopy (EDS) elemental mapping images for the piezo-component. f) XRD pattern for prepared KNNS ceramic. g) Electromechanical coupling coefficient k_{33} and acoustic impedance Z_a of the 1-3 piezocomposite as a function of ceramic volume fraction (line: theoretical prediction; symbols: experimental data). h) Impedance and phase angle spectra of the 1-3 piezocomposite before and after poling.

which satisfies an optimized ceramic volume fraction (≈60%) (Figure 2g). The developed piezocomposite exhibits a resonant frequency of 6.06 MHz (Figure 2h) and a lowered acoustic impedance Z_a (≈11.6 MRayl). The longitudinal electromechanical coupling k_{33} (≈0.70) and voltage coefficient g_{33} (≈38.3 × 10^{-3} V·m·N^{-1}) were substantially augmented by suppressing shear vibrating modes and lowering the permittivity,[28,37] effectively enhancing the sensitivity of the piezocomposite to receive ultrasound. The final microstructure piezoelectric component with a backing layer (300 μm) possesses a spatial volume of 1 mm × 1 mm × 0.6 mm (Figure 2d), enabling the miniaturization of the device. A summary of some important electrical and acoustic parameters of the ceramic/polymer piezocomposite and the pure KNNS ceramic are given in Table S1, Supporting Information. The detailed calculation and measurement methods are presented in Supporting Information and in Section 4.

A polyimide insulated copper wire with a diameter of 100 µm was used to fabricate flexible electrode to connect the piezoelectric component in the device and the external circuit (for the detailed fabrication process see Section 4). The accumulated electrons induced by piezoelectric effect can flow between the top and bottom electrodes through the external circuit.[38] The wavy structure design inspired by a stretchable ultrasonic device proposed by Wang et al. aims to accommodate the externally applied strain (Figure S3, Supporting Information).[23] The top and the bottom electrodes are routed to the same plane for optimized mechanical robustness. Finally, the entire device is encapsulated in a silicone elastomer (Ecoflex 00-10, Smooth-on Inc, Easton PA) with the Young's modulus (≈55 kPa) similar to that of human tissue (e.g., retina ≈20 kPa) (Figure 1b).[39,40] The thickness of the as-fabricated ultrasound patch is approximately 1.7 mm to balance the mechanical strength with acoustic receiving performance. The hydrophobicity of the silicone elastomer provides a barrier to moisture and protects the device from possible body fluid corrosion.[23] The Schematic illustration of the entire device fabrication process is shown in Figure S4, Supporting Information. Owing to its flexible mechanics, the ultrasound patch allows conformation to general complex surfaces (Figure 1c,d), showing its great potential for the application of implantable medical devices.

The working principle of an LF-PUEH device is demonstrated in **Figure 3**. Technically, the piezocomposite can be viewed as consisting of parallel-connected oscillator array,[41] which vibrates along the longitudinal *3-3* direction under the drive of ultrasound wave (see the schematic demonstrated in Figure 3a,b).[42] The impedance for an oscillator unit (Z_{j}, one ceramic pillar) and the whole 1-3 piezocomposite component ($\bar{Z}$) can be expressed respectively as[43]

$$Z_{\mathrm{j}} = -\frac{1}{i\omega C_0}\frac{\xi h\cot(\xi h) - e_{33}^2/\varepsilon_{33}\bar{C}_{33}}{\xi h\cot(\xi h)} \tag{6}$$

$$\frac{1}{\bar{Z}} = \sum_{j=1}^{n}\frac{1}{Z_{\mathrm{j}}} \tag{7}$$

wherein $C_0 = \frac{\varepsilon_{33}S}{2h}$, $\xi^2 = \frac{\rho\omega^2}{\bar{C}_{33}}$, and $\bar{C}_{33} = C_{33}\left(1+\frac{e_{33}^2}{\varepsilon_{33}c_{33}}\right)$. C_0 is the capacitance. C_{33}, ε_{33}, and e_{33} are the effective elastic, dielectric, and piezoelectric constants, respectively. ω, ρ, and ξ are the angular frequency, density, and wave number, respectively. S and h are the area and thickness of an oscillator unit Z_{j}, respectively. As shown in the equivalent circuit model in Figure 3b-ii, the oscillator array is equivalent to a current source. The current I_{j} flowing into the load Z_{L} from an oscillator unit Z_{j} and the total output voltage $\bar{V}$ applied to the load Z_{L} are derived respectively as[42]

$$I_{\mathrm{j}} = -\frac{Pk_{33}^2h}{e_{33}\left(1+k_{33}^2\right)}\frac{1}{\xi h\cot(\xi h)\left(Z_{\mathrm{j}}+Z_{\mathrm{L}}\right)} \tag{8}$$

$$\bar{V} = \sum_{j=1}^{n} I_{\mathrm{j}}Z_{\mathrm{L}} = -\frac{Pk_{33}^2h}{e_{33}\left(1+k_{33}^2\right)}\sum_{j=1}^{n}\frac{Z_{\mathrm{L}}}{\xi h\cot(\xi h)\left(Z_{\mathrm{j}}+Z_{\mathrm{L}}\right)} \tag{9}$$

wherein P is the ultrasonic pressure applied to the piezoelectric component and the time-harmonic factor exp ($i\omega t$) has been reduced to simplicity. When the load is equal to the internal impedance of the energy harvesting device, the maximum output power dissipated in the load is achieved.[42]

Simulations for the piezoelectric potential produced by the piezoelectric component that is placed in a focused acoustic field were conducted with a finite element analysis program (Comsol Multiphysics), as illustrated in Figure 3c. Since the whole device is in the acoustic medium, the ultrasonically induced mechanical deformation will occur throughout the device, including the piezoelectric layer. Polycrystalline ceramic pillars in the piezocomposite can produce charge dipoles that are linearly distributed due to the movement and switching of the polarization domains during the polling (Figure 3b-i).[44] When the piezocomposite is mechanically deformed, the piezoelectric potential is generated between the top and bottom electrodes due to the aligned dipoles. The potential distribution of 1-3 piezocomposite is represented by a color bar. Because of the insulating polymer filler and the silicone elastomer encapsulation, induced electrons flow through the external circuit to balance the generated piezoelectric field and accumulate at the interface of the bottom electrode. This behavior produces a signal of voltage and current (Figure 3c-iii). When the piezocomposite is subjected to a reverse acoustically driven pressure, the deformation and the potential are reversed. The accumulated electrons then flow back to the top electrode, thereby inducing an electrical signal in the opposite direction. In addition, the acoustic pressure near the transducer focal point is much higher than that at other points (Figure 3c). The energy is concentrated near the focal point. Therefore, the receiver should be placed near the focal point to effectively harvest the transmitted acoustic energy. A specific working process for the time-dynamic relationship between the piezoelectric potential and the ultrasonically driven pressure is illustrated in Video S1, Supporting Information. The results show that the 1-3 piezocomposite can convert ultrasonic energy into a piezoelectric potential as output.

To evaluate the output performance of the device, we measured the piezoelectric potentials produced by the ultrasonically driven LF-PUEH using a multifunctional testing platform (Figure S5, Supporting Information). First, the LF-PUEH device is an ultrasound receiver that converts the perceived ultrasonic signal into an electrical signal. Receiving is operated in a non-resonant mode which works well over a wide range of the band that is below its resonance frequency (the resonance frequency of our piezo-component is 6.06 MHz).[45] Apart from the sensitivity of the LF-PUEH itself, the outputs also depend on the strength of the received ultrasound signal. To excellently provide a penetrating ultrasonic signal to drive the LF-PUEH device, a kilohertz-level ring focused ultrasound transmitter (inner diameter: 9.5 mm, outer diameter: 28.5 mm, focal length: 20 mm) was designed and manufactured, as presented in **Figure 4**a (right inset). Transmitting is a resonant application that converts electricity to mechanical vibration, and optimal conversion efficiency is achieved when working near a resonant point.[46] The measured impedance and phase angle spectra of the transmitter are shown in Figure 4a, where a resonant frequency of 304 kHz was observed. The output

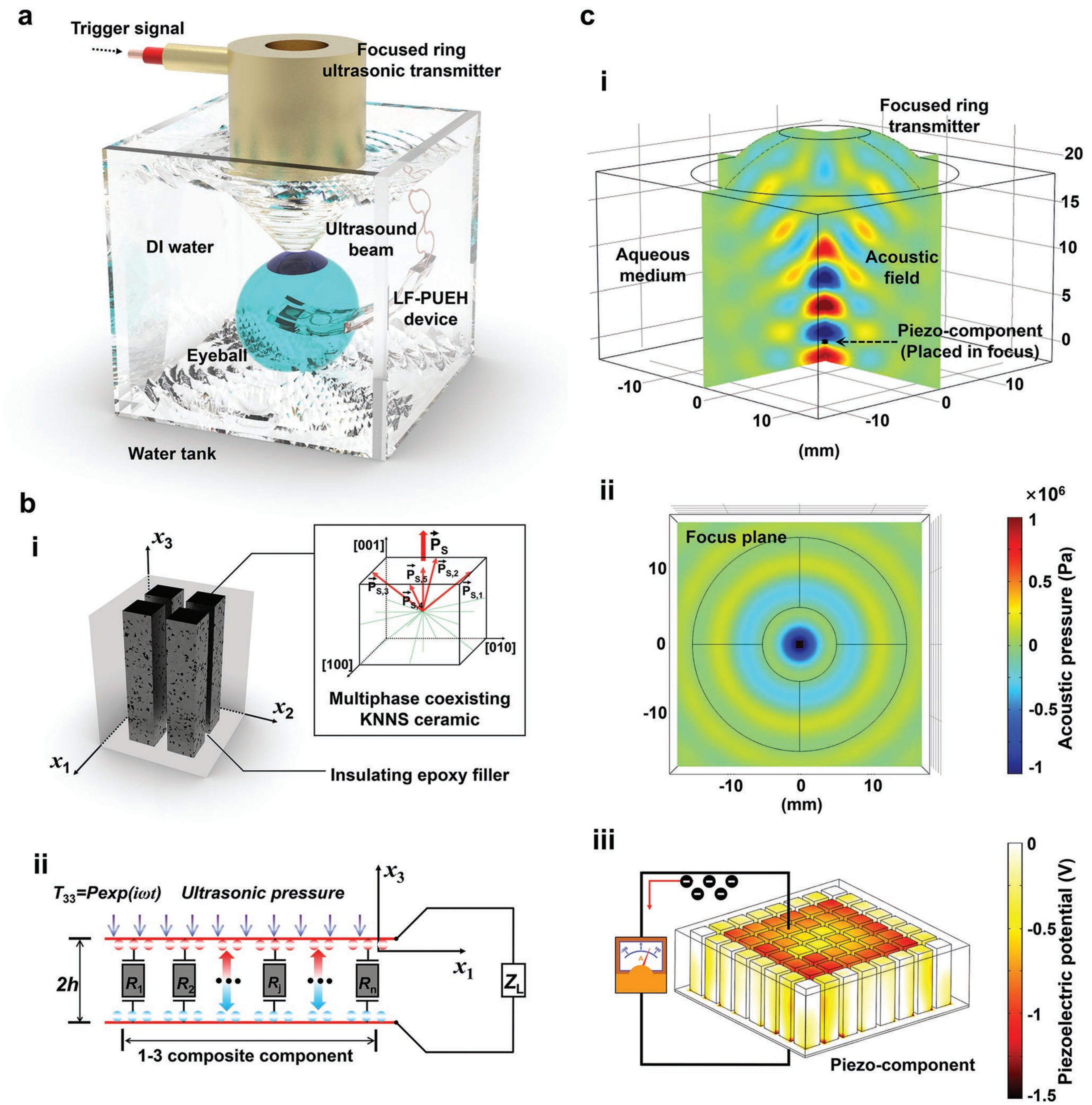

Figure 3. The working principle of the LF-PUEH device. a) Schematic illustration of a test setup. b) i: Schematic illustration of the 1-3 piezocomposite. The inset shows the schematic illustration for the spontaneous polarization in KNNS ceramic. The red arrows represent the possible directions of the polarization caused by an external electric field. ii: The equivalent circuit model for the LF-PUEH device. c) i: The simulated acoustic field of a focused transducer. ii: A section of the simulated acoustic field at the focal plane. iii: The simulated piezoelectric potential distribution inside a piezo-component induced by a focused ultrasonic field.

voltage amplitudes of the LF-PUEH device with different load resistances were measured by a burst-mode focused ultrasound driving over a wide frequency range (200–400 kHz) (Figure 4b). The results show that the maximum voltage is obtained at 304 kHz over the entire test range, corresponding to the resonance point of the transmitter. During the experiment, both the LF-PUEH device and the transmitter were immersed in deionized water with a fixed distance of 20 mm, which is the focal length of the transmitter and was calibrated by the time delay (≈26 µs) of pulse-echo response (Figure S6, Supporting Information).

Figure 4c shows the output voltage signals recorded as a function of the connected external resistance from 50 Ω to 1 MΩ to investigate the output power of the as-fabricated

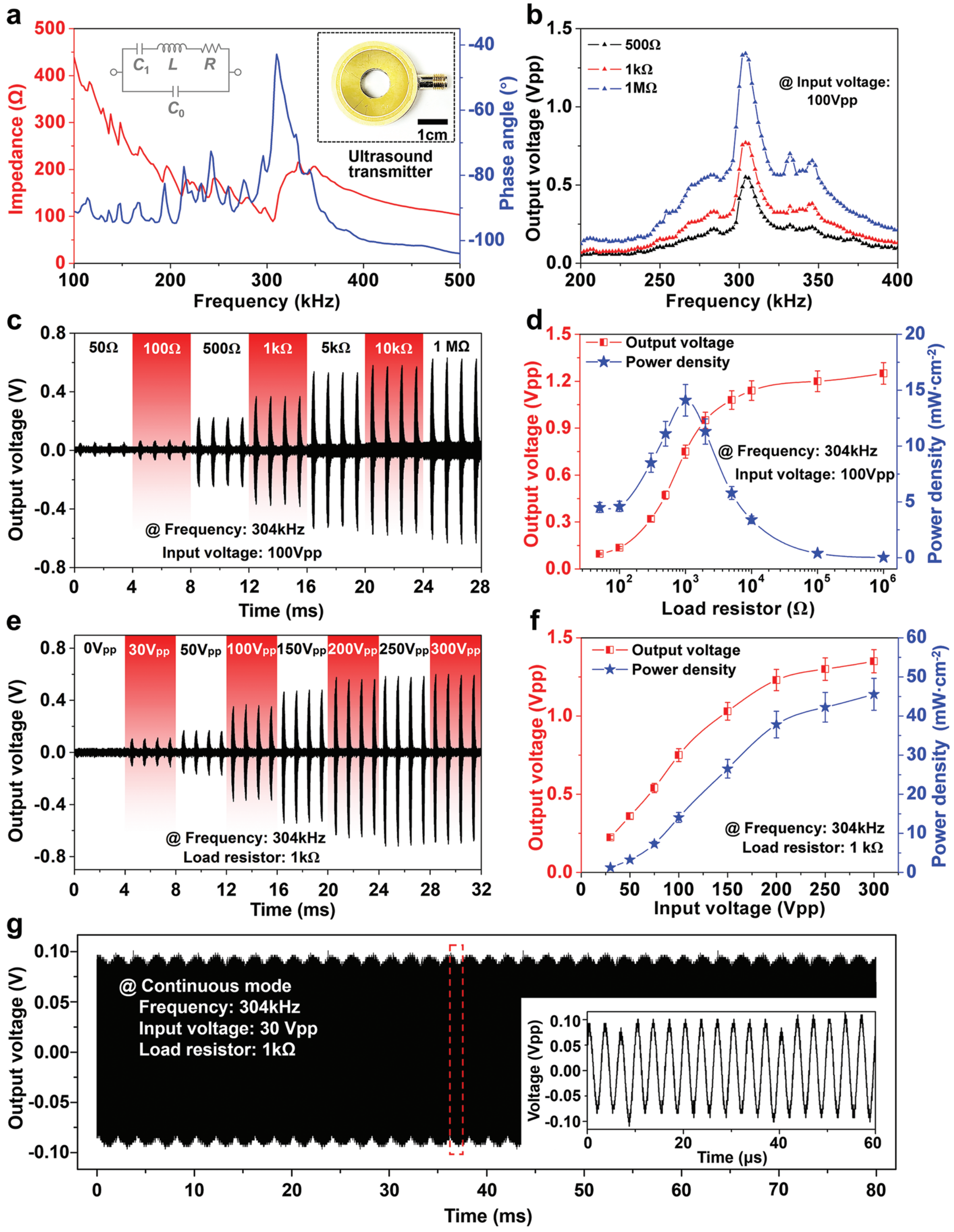

Figure 4. Electrical characterizations of the LF-PUEH device. a) Impedance and phase angle spectra of the ultrasound transmitter, showing a resonant frequency at 304 kHz. Left inset: equivalent inductance-capacitance-resistance circuit diagram of the ultrasound transmitter. Right inset: optical image of the ring focused ultrasound transmitter. b) Output voltage of the device with different loads as a function of frequency, showing an optimal output characteristic at 304 kHz. c) Output voltage amplitudes of the device with different loads. d) Output voltage and power density of the device as a function of load, respectively, showing an optimal output power at 1 kΩ. e) Output voltage amplitudes of the device at different input voltages. f) Output voltage and power density of the device as a function of input voltage, respectively. g) An output voltage signal of the device at a continuous-mode input signal (30 Vpp and 304 kHz). The inset shows the signal detail over a narrow time range. In the above burst-mode, the set parameters are as follows: cycle number, 50; trigger interval, 1 ms. The available time period is about 16%.

LF-PUEH device further. By increasing the load resistance, the voltage amplitudes through the resistor show a rising tendency and saturation at a higher external load. The instantaneous power output ($V_{\mathrm{pp}}^2/4Z_{\mathrm{L}}$) of the LF-PUEH device was estimated. As shown in Figure 4d, the maximal instantaneous power density of the device is 14.1 mW·cm^{-2} at an external load of 1 kΩ. An average impedance modulus at the electrode-retina interface is on the order of thousands of ohms.[47,48] The results indicate a good impedance matching between the developed device and the interface, which is beneficial to the application in implantable electrical stimulation. Further characterization is carried out by examining the input voltage dependence of the outputs at a load resistance of 1 kΩ. As displayed in Figure 4e, the voltage amplitudes increase and tend to saturate with increasing input voltage. The outputs cannot be significantly increased when further increasing the input voltage (>200 Vpp). The thermal effects and the cavitations in the liquid caused by high energy ultrasound will lead to additional energy losses, resulting in a reduction in efficiency. The wireless energy transfer system can effectively produce considerable outputs, reaching a maximum power density of 45 mW·cm^{-2} (Figure 4f). The results demonstrate that the LF-PUEH device is superior to other UEHs,[12,49–51] and even comparable to some traditional generators using mechanical vibration.[52–54] In the above burst-mode ultrasonically driven measurements, an obvious ring-down time range caused by the back reflections of ultrasound was observed from the waveform of the output signal (Figure S8, Supporting Information), which indicates that the output signals of the LF-PUEH device are induced by the ultrasonic drive rather than the leakage behavior at the input.[55] To further confirm that the output signals are purely induced by the piezoelectric effect of the piezocomposite component, a continuous-mode sinusoidal signal (30 Vpp and 304 kHz) (Figure S7, Supporting Information) was switched to trigger the transmitter. The measured output produced from the LF-PUEH device is correspondingly a continuous sinusoidal signal (Figure 4g). Additionally, we have evaluated the pure silicone elastomer that does not contain piezocomposite component and no reliable signals were observed, as displayed in Figure S9, Supporting Information. The results further indicate that the outputs are produced from charges induced by the strain of the piezoelectric component in the device during the ultrasonic propagation.

To utilize the LF-PUEH device as an additional wireless power source for an implantable medical device, it is necessary to achieve high electric power from the transmitted ultrasound and store or deliver the generated electricity. Here, an application of the ultrasonic energy harvesting technology to power commercial micro-devices is demonstrated. The alternating current (AC) peak generated by the LF-PUEH device is not compatible with the direct current (DC) system of general electronic equipment. The AC signal was therefore rectified into a common DC signal by a predesigned full-wave-bridge-rectification circuit (**Figure 5**a). The rectified signal of the LF-PUEH device was measured and stored into a 220 µF capacitor (Figure 5b). The voltage stored on the capacitor increased to 540 mV during the charging process triggered by the 304 kHz burst-mode focused ultrasound for 200 s (Figure 5c). The average charging power $\overline{P}$ was evaluated in the process, which is given by[49]

$$\overline{P} = \frac{C_S V^2}{2T} \tag{10}$$

wherein C_{S} is the capacitance, T is the charging time and V is the stored voltage. Thus, the energy stored on the storage capacitor was increased by 32.08 µJ in 200 s, indicating that the power output capability of the LF-PUEH device is 160.38 nW, which is well above the previously reported results (20–40 nW) of UEHs (see Table S2, Supporting Information; Figure 5d).[12,49,56,57] By connecting the five charged capacitors in series, the total available voltage is about 2.3 V (Figure S10, Supporting Information), which is enough to power some commercial micro-devices. As demonstrated in Figure 5e, the energy harvested from the ultrasound was used to operate a commercial red light-emitting diode (LED). As a conclusion, the commercial LED was successfully lit up by the energy generated from the LF-PUEH device without any additional power supplies, showing great potential as the wireless power source for the next-generation implantable medical devices.

To demonstrate the feasibility of embedding LF-PUEH in the body, ex vivo experiment of the implant device was performed. **Figure 6**a shows the schematic profile of the working principle. A primary design goal for an ultrasonically powered implant is to minimize power losses, mainly including beam divergence, pressure wave reflection, tissue absorption, and piezoelectric coupling.[58] First, a focused ultrasonic transmitter which can improve the energy utilization by concentrating the acoustic beam to a smaller area was adopted in this study. Second, a reflection of ultrasound off the surface of the tissue is due to acoustic impedance mismatch between the aqueous medium (or coupling agents) (Z_{a} ≈ 1.5 MRayl) and tissue (Z'_{a} ≈ 1.70 MRayl).[12,59] The power reflected from the tissue surface is given in[60]

$$\frac{P_{\text{reflected}}}{P_{\text{tissue face}}} = \left(\frac{Z'_{\mathrm{a}} - Z_a}{Z'_{\mathrm{a}} + Z_a}\right)^2 \tag{11}$$

Due to the similar acoustic impedance, the loss (≈0.4%) caused by the tissue reflection is very weak and negligible. Third, the power absorption is heavily dependent on the acoustic frequency and penetration depth, which is given by[60]

$$\frac{P_{\text{absorbed}}}{P_{\text{source}}} = 1 - e^{-2\alpha_0 f^n d} \tag{12}$$

As the ultrasonic frequency increases linearly, the remaining ultrasonic power decreases exponentially after traveling through the tissue. Thus, a low-frequency ultrasound (304 kHz) is used in this work to reduce power losses due to absorption. Fourth, piezoelectric coupling is an inherent property of a material, which can be improved by designing and fabricating the 1-3 type piezocomposite component. In summary, several key components have been optimized in this work in order to present a better ultrasonically powered system. Its performance

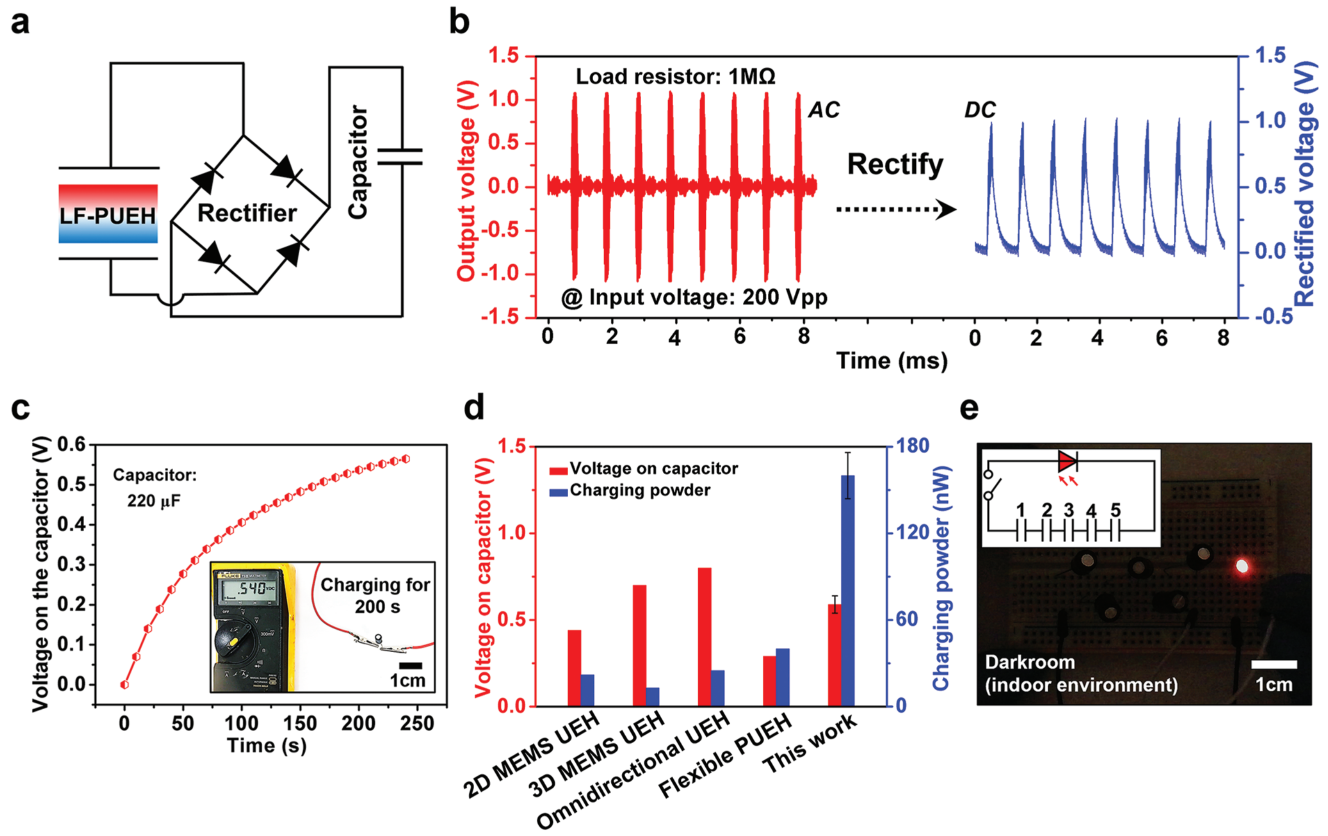

Figure 5. Applications of the LF-PUEH device on microelectronic devices. a) A circuit schematic for charging a capacitor using the device. The full-wave-bridge-rectification circuit composes of four diodes. b) Output voltage amplitudes before (left) and after (right) rectification of the device. c) The charging time dependence of voltage on a 220 µF capacitor; the inset shows the measured voltage (≈0.540 V) charged for 200 s. d) Comparison of the average charging power of UEHs. e) Optical image showing a commercial LED lit up by the electricity stored in capacitors. The inset shows a schematic circuit diagram of five capacitors in serial.

has been validated by our measurement results. Figure 6b,c show the experimental setup, in which the device is implanted into an excised porcine eyeball from a local slaughterhouse (Sierra Medical Science, Inc., Whittier, CA, USA) to mimic an implant situation. The results of voltage amplitudes as a function of inputs are shown in Figure 6d. There is a slight drop in voltage amplitudes for the device in the implanted environment. For example, the voltage amplitude reaches 0.54 Vpp at the input voltage of 100 Vpp and a load of 1 kΩ, and the corresponding power density is 7.3 mW·cm^{-2} (Figure 6e), which are 72% and 52% of the values (0.75 Vpp and 14.1 mW·cm^{-2}) in the non-planted case, respectively (Figure 6f). The results show that the proposed LF-PUEH device can harvest considerable energy when implanted in biological tissue, and thus can be developed into a wireless power source for a series of biological implants, such as retinal electrical stimulators.

For practical retinal electrical stimulation applications, current parameters are of particular interest, for example, the average threshold current or threshold current density.[2,61] To discuss data from this work in the context of previous studies, a systematic review of the published literature was composed. More than 30 works on epiretinal stimulation thresholds were summarized, as presented in Table S3, Supporting Information. These works span several orders of magnitude in electrode size and can therefore be used to elucidate the threshold trends. To facilitate the discussion, the threshold parameters against the geometric electrode surface areas have been plotted in **Figure 7**, along with best fit-lines. The threshold current decreases dramatically when the electrode size is reduced (Figure 7a). The trend confirms that a smaller electrode requires several orders of magnitude lower current to elicit responses. Nevertheless, the current density increases somewhat as the electrode size is reduced (Figure 7b). Thus, tailoring the electrode size to achieve a parameter above the threshold can be a strategy in stimulation applications where the output current is constant. A 100 µm diameter flexible electrode possessing an electrode surface area of about 7.85 × 10^3 µm^2 was used in this work. Representative data which were obtained by the Ohm's law ($V_O = I_O Z_L$) in the ex vivo experiment are shown in Figure 7. For example, a current of 72 µA and a current density of 9.2 nA·µm^{-2} can be obtained at the input voltage of 30 Vpp, which are higher than the average threshold required for retinal electrical stimulation.[2] Additionally, the output value is flexibly adjustable over a wide range to meet different applications, reaching a maximum current density of 54.5 nA·µm^{-2}. The results show great potential to be integrated on a future generation of the implantable biomedical device for electrical stimulation application.

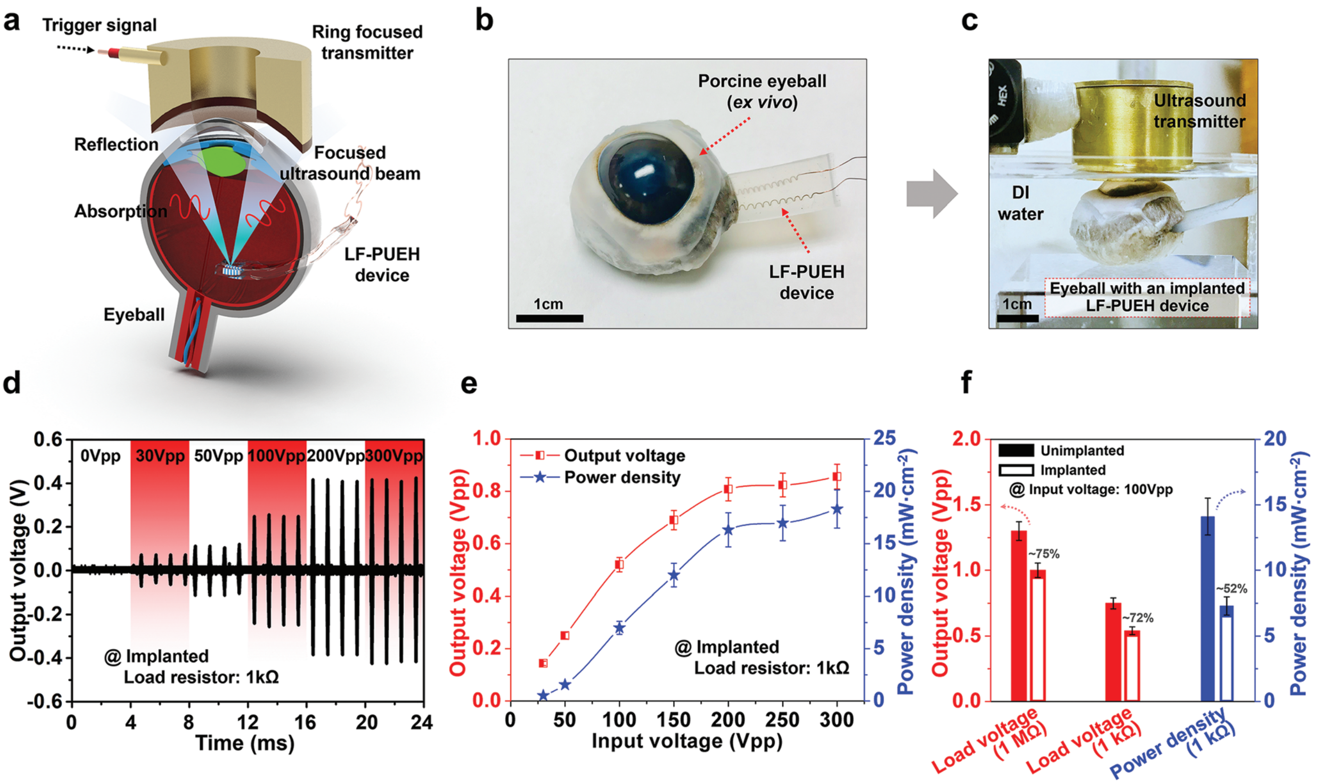

Figure 6. Evaluation of the LF-PUEH device in the ex vivo experiment of an implanted environment. a, b) Schematic profile and optical image of the device implanted into an excised eyeball to mimic an implant situation, with key components labeled. c) Optical image showing the experimental setup. d) Output voltage amplitudes of the device at different input voltages. e) Output voltage and power density of the device as a function of input voltage, respectively. f) Comparison of output voltages and power densities of the device in the case of implantation and non-implantation.

In this work, an electrical stimulation strategy was proposed using ultrasound-driven wireless energy harvesting technology. Although the results indicate the feasibility of ultrasound-induced electrical stimulation, ultrasound-related biological effects are worth discussing. High ultrasound energy exerts important cellular, genetic, thermal, and mechanical effects. For example, heat produces a wide variety of tissue injury including necrosis and apoptosis, abnormal cell migration, altered gene expression, and membrane dysfunction.[62] Here, the temperature changes of local tissue were measured in real time in an ex vivo experiment, as shown in Figure S11, Supporting Information. The results show no significant temperature elevation caused by ultrasound. As an example, a maximum temperature difference of 0.6 °C is obtained after 5 min by the excitation voltage at 300 Vpp. Additionally, ultrasound energy creates mechanical forces independent of thermal effects, thereby

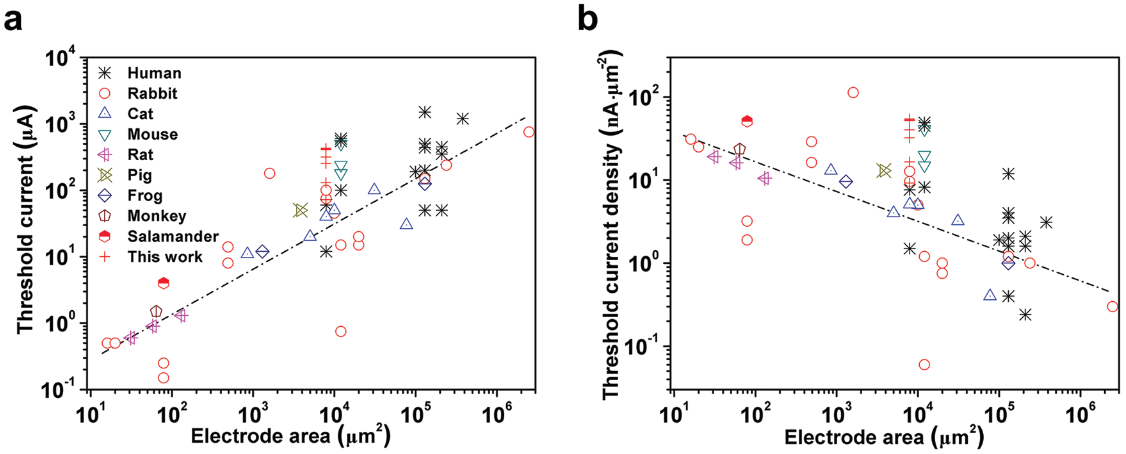

Figure 7. Analysis of thresholds for retinal electrical stimulation. a) Threshold current plotted against electrode area. b) Threshold current density plotted against electrode area. The data are from previously published literature, and dashed lines are best fits to the data.

causing biologic effects that are not related to temperature rise alone (termed nonthermal). The mechanical effects result in shear forces, pressure changes, and release of various reactive molecules.[62] Therefore, higher intensity ultrasound combined with longer duration of exposure may cause detrimental effects. We used pulsed ultrasound to avoid this problem. The potential for ultrasound to cause adverse effects in experimental animals is well established in previous studies.[62] Currently, the FDA stipulates that diagnostic ultrasound scanners for general human tissue cannot exceed a mechanical index (MI) of 1.9.[20] MI is an ultrasound metric. It is defined as[63]

$$\mathrm{MI} = \frac{\mathrm{PNP}}{\sqrt{F_c}} \tag{13}$$

where PNP is the peak negative pressure of the ultrasound wave (MPa) and F_c is the center frequency of the ultrasound wave (MHz). In this work, the ring transmitter at 304 kHz was excited in a burst-mode (cycle number: 50; trigger interval: 1 ms). According to the output tests and simulation, the MI was calculated to be 1.81 for an excitation voltage of 200 Vpp. The intensity of the acoustic wave is proportional to the excitation voltage. Considering the electrical stimulation threshold and FDA standards, therefore, a range of 30–200 Vpp is recommended for general implantable applications. The eye is the most important sensory organ of the human body, which is more sensitive to ultrasound. Previous studies have shown that intense-focused ultrasound could cause heat injury, leads to an acute increase in intraocular pressure. Heat damage in zonular fibers could cause accommodation spasm.[64] Finally, some suggestions about possible research approaches and potential methodologies are provided, which could be profitably utilized in minimizing the ultrasonic biological effects of ophthalmology field. First, an excitation voltage as low as possible is used while satisfying the threshold. As an example, a range of 30–50 Vpp is recommended for the ultrasound-induced retinal electrical stimulation proposed herein. Second, the pulsed ultrasound is used for the energy transfer to avoid the concentrated release of ultrasonic energy in a short duration. Third, the energy conversion efficiency can be improved by the material and structure design. If the receiving sensitivity is improved, the organism can be interrogated under lower acoustic energy and the ultrasonic biological effects can be minimized.

3. Conclusion

In summary, a potential electrical stimulation strategy using ultrasound-driven wireless energy transfer technology was presented to convert acoustic energy into electricity through an mm-scale ultrasonic energy harvesting device that is flexible and lead-free. In this delicate architecture, the electromechanical coupling performance is improved by the design of a microscale piezocomposite. Meanwhile, the device is designed to be flexible to attach on complex surfaces required in bioimplantable applications. The principle of power generation and the role of piezocomposite in LF-PUEH device have been theoretically analyzed. The as-developed device can be driven by ultrasound to produce adjustable electrical outputs, reaching a maximum output power of 45 $\mathrm{mW \cdot cm^{-2}}$. The rectified energy generated from the device is stored in capacitors that are demonstrated to be subsequently used to operate a commercial LED device. The considerable current signals (e.g., current > 72 μA, and current density > 9.2 $\mathrm{nA \cdot \mu m^{-2}}$), which are higher than the average thresholds of retinal electrical stimulation, are also obtained in the ex vivo experiment of an implanted environment. The ultrasound-driven wireless energy transfer system innovatively expands the feasibility of using medical electrical stimulation in more general applications.

4. Experimental Section

Fabrication of the Lead-Free Piezoelectric 1-3 Composite: $(\mathrm{K_{0.48}Na_{0.52}})(\mathrm{Nb_{0.95}Sb_{0.05}})\mathrm{O_3}$-$(\mathrm{Bi_{0.4}La_{0.1}})(\mathrm{Na_{0.4}Li_{0.1}})\mathrm{ZrO_3}$ (abbreviated as KNNS) lead-free piezoelectric ceramic was synthesized using the conventional solid-state sintering technology.[65] Bi_2O_3 (99.999%), La_2O_3 (99.9%), K_2CO_3 (99%), Na_2CO_3 (99.8%), Sb_2O_3 (99.99%), Li_2CO_3 (98%), Nb_2O_5 (99.5%), and ZrO_2 (99%) were the raw materials. A modified dice-and-fill technique (Tcar 864-1, Thermocarbon) was employed to manufacture the microstructure 1-3 ceramic/polymer piezocomposite formed by a regular-shaped ceramic pillar (85 × 85 μm^2) array and small kerf (25 μm), as illustrated in Figure 2 and Figure S2, Supporting Information. Insulating epoxy (EPO-TEK 301, Epoxy Technology) was applied to fill the kerfs. Then, both sides of the lapped composite sample (300 μm) were mechanically polished and sputtered with Cr/Au (50/100 nm) electrodes using a sputtering system (NSC-3000 Sputter Coater, Nano-Master). Material as the backing layer (300 μm) (E-Solder 3022, Von Roll Isola) was cured on the bottom side of the prepared composite sample. After curing, the whole acoustic stack was diced into small posts with an aperture size of 1 mm × 1 mm. Finally, poling was carried out for 15 min at 3 $\mathrm{kV \cdot cm^{-1}}$ (direct current) to achieve the acoustic–electric conversion capability of the piezoelectric elements.

Fabrication of the Flexible LF-PUEH Device: The process can be summarized into three parts (Figure S3, Supporting Information; Figure 4): 1) flexible electrode manufacturing, 2) electrode transferring, and 3) soft elastomeric encapsulating. In this work, a 100 μm diameter copper wire was selected as the flexible external electrode. First, the wire wrapped equidistantly around a 500 μm diameter stainless-steel needle by a lathe (SD 400, PRAZI). The "helical-structure" was then removed from the needle and placed flat on a water platform. The straight "helical-structure" copper wire was pressed into a flat plane using a polished ingot to achieve flexible wavy electrodes. After that, both the top and bottom flexible electrodes and copper foil electrodes (diameter 1 mm, thickness 1 μm) were bonded on the prepared acoustic post by a conductive silver paste (E-Solder 3022). The LF-PUEH device was then encapsulated in a silicone elastomer (Ecoflex 00-10, Smooth-on Inc, Easton PA) after plasma cleaning. Curing was carried out for 2 h at room temperature, and the slides were then peeled off, yielding a freestanding flexible LF-PUEH device.

Material Characterization: X-ray diffraction (XRD, DX2700) was carried out to determine the crystal structure of the prepared KNNS ceramic sample. The surface morphology and energy dispersive spectroscopy (EDS) were analyzed by a field emission scanning electron microscopy (FE-SEM, JSM-7500). Impedance spectrum of the 1-3 composite was determined by an impedance analyzer (4294A, Agilent) (Figure 2h). The piezoelectric constant d_{33} was characterized by a d_{33} meter (YE2730A, APC Products). The capacitance was determined by an inductance-capacitance-resistance digital bridge instrument (1715 LCR, QuadTech). According to the *IEEE* standard on piezoelectricity,[66] the piezoelectric voltage coefficient g_{33} and electromechanical coupling coefficient k_{33} are given respectively by

$$g_{33} = \frac{d_{33}}{\varepsilon_{33}^{T}} \tag{14}$$

$$k_{33} = \sqrt{\frac{\pi}{2}\frac{f_\mathrm{r}}{f_\mathrm{a}}\tan\left(\frac{\pi}{2}\frac{f_\mathrm{a}-f_\mathrm{r}}{f_\mathrm{a}}\right)} \tag{15}$$

wherein the f_r (≈6.06 MHz) and f_a (8.10 MHz) are the resonant frequency and anti-resonant frequency, respectively. Some important acoustic and electric parameters of the KNNS ceramic and 1-3 composite are summarized in Table S1, Supporting Information.

Electrochemical Properties Evaluation: The outputs of the LF-PUEH device were characterized by a multifunctional testing platform (Figure S5, Supporting Information). A ring focused transducer as the ultrasound transmitter was mounted on a 5-axis machine (OptoSigma). The LF-PUEH device as an ultrasound receiver was placed about 20 mm away from the end face of the transmitter. The transmitter was triggered by a sinusoidal signal that was provided by an arbitrary function generator (AFG3252C, Tektronix) and then amplified by an amplifier (75A250A, AR RF/Microwave Instrumentation). The output voltage amplitudes produced by the LF-PUEH device were determined by an oscilloscope (TDS 5052, Tektronix). The temperature changes of local tissue were measured in real time in the ex vivo experiment through inserting a thermocouple (Digital Thermometer, 6802 II, Signstek) into the tissue. The thermocouple is tightly close to the LF-PUEH device that is placed near the focal point of the transmitter.

Supporting Information

Supporting Information is available from the Wiley Online Library or from the author.

Acknowledgements

This work was partially supported by the National Institutes of Health (NIH) under grants 1R01EY026091, R01 EY028662, and R01 HL127271; the National Science Foundation (NSF) under grants CMMI 1335476 and CMMI 1663663; and an unrestricted grant to the Department of Ophthalmology from Research to Prevent Blindness, New York. L.J. was supported by the China Scholarship Council (File no.: 201706240056).

Conflict of Interest

The authors declare no conflict of interest.

Keywords

biomedical, flexible device, piezoelectric composite, retinal stimulation, ultrasonic energy transfer

Received: March 27, 2019
Revised: April 26, 2019

---

[1] D. C. Rodger, A. J. Fong, W. Li, H. Ameri, A. K. Ahuja, C. Gutierrez, I. Lavrov, H. Zhong, P. R. Menon, E. Meng, *Sens. Actuators, B* **2008**, *132*, 449.
[2] C. Sekirnjak, P. Hottowy, A. Sher, W. Dabrowski, A. Litke, E. Chichilnisky, *J. Neurophysiol.* **2006**, *95*, 3311.
[3] B. Roska, J.-A. Sahel, *Nature* **2018**, *557*, 359.
[4] E. Margalit, S. R. Sadda, *Artif. Organs* **2003**, *27*, 963.
[5] J. D. Weiland, M. S. Humayun, *Proc. IEEE* **2008**, *96*, 1076.
[6] A. T. Chuang, C. E. Margo, P. B. Greenberg, *Brit. J. Ophthalmol.* **2014**, *98*, 852.
[7] K. Bazaka, M. V. Jacob, *Electronics* **2012**, *2*, 1.
[8] J. Charthad, M. J. Weber, T. C. Chang, A. Arbabian, *IEEE J. Solid-State Circuits* **2015**, *50*, 1741.
[9] W. Biederman, D. J. Yeager, N. Narevsky, J. Leverett, R. Neely, J. M. Carmena, E. Alon, J. M. Rabaey, *IEEE J. Solid-State Circuits* **2015**, *50*, 1038.
[10] J. M. Rabaey, M. Mark, D. Chen, C. Sutardja, C. Tang, S. Gowda, M. Wagner, D. Werthimer, presented at the *Design, Automation and Test in Europe Conf. and Exhibition (DATE)*, Grenoble, France, March **2011**.
[11] D. Seo, R. M. Neely, K. Shen, U. Singhal, E. Alon, J. M. Rabaey, J. M. Carmena, M. M. Maharbiz, *Neuron* **2016**, *91*, 529.
[12] L. Jiang, Y. Yang, R. Chen, G. Lu, R. Li, D. Li, M. S. Humayun, K. K. Shung, J. Zhu, Y. Chen, *Nano Energy* **2019**, *56*, 216.
[13] P. Gélat, G. Ter Haar, N. Saffari, *Phys. Med. Biol.* **2012**, *57*, 8471.
[14] M. D. Menz, Ö. Oralkan, P. T. Khuri-Yakub, S. A. Baccus, *J. Neurosci.* **2013**, *33*, 4550.
[15] A. Y. Cheung, A. Neyzari, *Cancer Res.* **1984**, *44*, 4736s.
[16] K. G. Baker, V. J. Robertson, F. A. Duck, *Phys. Ther.* **2001**, *81*, 1351.
[17] I. Rosenthal, J. Z. Sostaric, P. Riesz, *Ultrason. Sonochem.* **2004**, *11*, 349.
[18] D. L. Miller, N. B. Smith, M. R. Bailey, G. J. Czarnota, K. Hynynen, I. R. S. Makin, Bioeffects Committee of the American Institute of Ultrasound in Medicine, *J. Ultrasound Med.* **2012**, *31*, 623.
[19] M. Tanter, M. Fink, *IEEE Trans. Sonics Ultrason.* **2014**, *61*, 102.
[20] U. Food, D. Administration, Rockville, MD: Center for Devices and Radiological Health, US Food and Drug Administration, **1997**.
[21] J. C. Lin, *IEEE Antennas Propag. Mag.* **2006**, *48*, 157.
[22] B. C. Johnson, K. Shen, D. Piech, M. M. Ghanbari, K. Y. Li, R. Neely, J. M. Carmena, M. M. Maharbiz, R. Muller, paper presented at the *IEEE Custom Integrated Circuits Conf. (CICC)*, San Diego, CA, April **2018**.
[23] C. Wang, X. Li, H. Hu, L. Zhang, Z. Huang, M. Lin, Z. Zhang, Z. Yin, B. Huang, H. Gong, *Nat. Biomed. Eng.* **2018**, *2*, 687.
[24] L. Tacchetti, W. A. Serdijn, V. Giagka, paper presented at the *IEEE Biomedical Circuits and Systems Conf. (BioCAS)*, Cleveland, OH, October **2018**.
[25] W. Qiu, J. Zhou, Y. Chen, M. Su, G. Li, H. Zhao, X. Gu, D. Meng, C. Wang, Y. Xiao, *IEEE Trans. Neural Syst. Rehabil. Eng.* **2017**, *25*, 2509.
[26] H. Hu, X. Zhu, C. Wang, L. Zhang, X. Li, S. Lee, Z. Huang, R. Chen, Z. Chen, C. Wang, *Sci. Adv.* **2018**, *4*, eaar3979.
[27] Z.-Y. Shen, Y. Xu, J.-F. Li, *J. Appl. Phys.* **2009**, *105*, 104103.
[28] H. L. W. Chan, J. Unsworth, *IEEE Trans. Sonics Ultrason.* **1989**, *36*, 434.
[29] E. Directive, *Off. J. L* **2002**, *37*, 13.
[30] G. Vats, R. Vaish, *Int. J. Appl. Ceram. Technol.* **2014**, *11*, 883.
[31] S. Chen, C. K. I. Tan, S. Y. Tan, S. Guo, L. Zhang, K. Yao, *J. Am. Ceram. Soc.* **2018**, *101*, 5524.
[32] J. Xing, Z. Tan, L. Jiang, Y. Wu, Y. Yue, Q. Chen, J. Wu, W. Zhang, D. Xiao, J. Zhu, *Appl. Phys. Lett.* **2017**, *110*, 022905.
[33] F. Z. Yao, K. Wang, W. Jo, K. G. Webber, T. P. Comyn, J. X. Ding, B. Xu, L. Q. Cheng, M. P. Zheng, Y. D. Hou, *Adv. Funct. Mater.* **2016**, *26*, 1217.
[34] Z. Y. Shen, J. F. Li, R. Chen, Q. Zhou, K. K. Shung, *J. Am. Ceram. Soc.* **2011**, *94*, 1346.
[35] A. Selfridge, G. Kino, B. Khuri-Yakub, paper presented at the *IEEE Ultrasonics Symp.*, Boston, MA, November **1980**
[36] X. Geng, Q. Zhang, *J. Appl. Phys.* **1999**, *85*, 1342.
[37] W. A. Smith, *IEEE Trans. Sonics Ultrason.* **1993**, *40*, 41.
[38] K. I. Park, C. K. Jeong, J. Ryu, G. T. Hwang, K. J. Lee, *Adv. Energy Mater.* **2013**, *3*, 1539.
[39] *Ecoflex Product Datasheet*, www.smooth-on.com/tb/files/ECOFLEX_SERIES_TB.pdf (accessed: December 2018).
[40] I. Jones, M. Warner, J. Stevens, *Eye* **1992**, *6*, 556.
[41] Y. Sun, X. Gao, H. Wang, Z. Chen, Z. Yang, *Appl. Phys. Lett.* **2018**, *112*, 043903.

[42] Z. Yang, D. Zeng, H. Wang, C. Zhao, J. Tan, *Smart Mater. Struct.* **2015**, *24*, 075029.
[43] Z. Yang, H. Wang, C. Zhao, D. Zeng, *Philos. Mag. Lett.* **2015**, *95*, 324.
[44] L. Jiang, Z. Tan, L. Xie, Y. Li, J. Xing, J. Wu, Q. Chen, D. Xiao, J. Zhu, *J. Eur. Ceram. Soc.* **2018**, *38*, 2335.
[45] L. Ivey, *NRL-USRD series F42 omnidirectional standard transducers*: Naval Research Laboratory, Underwater Sound Reference Detachment, **1979**.
[46] K. K. Shung, M. Zippuro, *IEEE Eng. Med. Biol. Mag.* **1996**, *15*, 20.
[47] S. Shah, A. Hines, D. Zhou, R. J. Greenberg, M. S. Humayun, J. D. Weiland, *J. Neural Eng.* **2007**, *4*, S24.
[48] A. Ray, L. L.-h. Chan, A. Gonzalez, M. S. Humayun, J. D. Weiland, *IEEE Trans. Neural Syst. Rehabil. Eng.* **2011**, *19*, 696.
[49] A. G. Fowler, S. Moheimani, S. Behrens, *J. Microelectromech. Syst.* **2014**, *23*, 1454.
[50] Q. Shi, T. Wang, C. Lee, *Sci. Rep.* **2016**, *6*, 24946.
[51] Q. Shi, T. Wang, T. Kobayashi, C. Lee, *Appl. Phys. Lett.* **2016**, *108*, 193902.
[52] S. Lee, Q. Shi, C. Lee, *APL Mater.* **2019**, *7*, 031302.
[53] F. Hu, Q. Cai, F. Liao, M. Shao, S. T. Lee, *Small* **2015**, *11*, 5611.
[54] J. Choi, I. Jung, C.-Y. Kang, *Nano Energy* **2019**, *56*, 169.
[55] D. Zhou, K. H. Lam, Y. Chen, Q. Zhang, Y. C. Chiu, H. Luo, J. Dai, H. L. W. Chan, *Sens. Actuators, A* **2012**, *182*, 95.
[56] Y. Zhu, S. R. Moheimani, M. R. Yuce, *IEEE Sens. J.* **2011**, *11*, 155.
[57] A. G. Fowler, S. R. Moheimani, S. Behrens, paper presented at the *IEEE Sensors*, Taipei, Taiwan, October **2012**.
[58] D. B. Christensen, S. Roundy, *J. Intell. Mater. Syst. Struct.* **2016**, *27*, 1092.
[59] M. G. Roes, J. L. Duarte, M. A. Hendrix, E. A. Lomonova, *IEEE Trans. Ind. Electron.* **2013**, *60*, 242.
[60] D. A. Christensen, *Ultrasonic Bioinstrumentation*, Wiley,New York **1988**.
[61] S. F. Cogan, *Annu. Rev. Biomed. Eng.* **2008**, *10*, 275.
[62] H. Shankar, P. S. Pagel, *Anesthesiology* **2011**, *115*, 1109.
[63] T. L. Szabo, *Diagnostic Ultrasound Imaging: Inside Out*, Academic Press,Cambridge, MA **2004**.
[64] Y. Chen, Z. Shi, Y. Shen, *BMC Ophthalmol.* **2018**, *18*, 214.
[65] L. Jiang, J. Xing, Z. Tan, J. Wu, Q. Chen, D. Xiao, J. Zhu, *J. Mater. Sci.* **2016**, *51*, 4963.
[66] T. Meeker, *IEEE Trans. Sonics Ultrason.* **1996**, *43*, 717.